Two-dimensional ferroelectric crystal with temperature-invariant ultralow thermal conductivity

Wenjie Zhou, ^{1,2,*} Changming Ke, ^{2,3,*} and Shi Liu ^{0,2,3,†}

¹Zhejiang University, Hangzhou, Zhejiang 310058, China

²Department of Physics, School of Science, Westlake University, Hangzhou, Zhejiang 310030, China

³Institute of Natural Sciences, Westlake Institute for Advanced Study, Hangzhou, Zhejiang 310024, China

(Received 17 January 2025; revised 30 September 2025; accepted 1 October 2025; published 15 October 2025)

We report the discovery of temperature-invariant ultralow thermal conductivity (κ) in monolayer β' -In₂Se₃, a two-dimensional ferroelectric crystal with in-plane polarization. Using a combination of generalized Wigner transport equation theory and machine-learning-assisted molecular dynamics simulations, we reveal that the balance between particlelike phonon propagating and wavelike tunneling transport mechanisms results in a propagating-tunneling-invariant ultralow thermal conductivity of approximately 0.6 W/mK (comparable to that of glass) over a broad temperature range (150 < T < 800 K). This behavior stems from intrinsic strong lattice anharmonicity driven by ferroelectric dipolar fluctuations, eliminating the need for extrinsic structural modifications. In contrast, the α -In₂Se₃ monolayer, which shares the same stoichiometry, exhibits a temperature-dependent thermal conductivity typical of simple crystals. We show that the anharmonicity in β' -In₂Se₃ can be precisely modulated by an external electric field, enabling on-demand control of the temperature scaling behavior of heat conductivity. Furthermore, an electric-field-driven motion of the α/β' phase interface is demonstrated, supporting a nonvolatile, large thermal switching ratio of >3. These findings provide fundamental insights into the interplay between field-tunable lattice anharmonicity, phonon dynamics, and thermal transport mechanisms.

DOI: 10.1103/3nqr-9b32

I. INTRODUCTION

Thermal conductivity (κ), a fundamental property of materials, is crucial in both scientific research and technological applications as it quantifies the efficiency of thermal energy transfer. Investigating its temperature (T) dependence helps elucidate transport mechanisms that differentiate metals, semiconductors, and insulators, as well as detect phase transitions [1]. Effective thermal management is essential for industrial energy use [2], improving electronic device performance [3,4], and advancing renewable energy technologies [5,6].

The theoretical framework for understanding thermal conductivity has evolved from Peierls's Boltzmann transport equation (BTE) [7] to the Allen-Feldman (AF) model [8] and, more recently, to the generalized Wigner transport equation (WTE) [9]. Grounded primarily in quasiharmonic approximations of lattice vibrations, the BTE framework describes heat conduction in ordered crystals by treating phonons as particlelike entities undergoing diffuse and scattering affected by anharmonic interactions [7]. This approach often predicts a $\kappa(T) \propto T^{-1}$ relationship when three-phonon processes dominate thermal resistance. In contrast, the AF model is a harmonic theory of thermal transport in glasses where heat diffuses in a wavelike fashion through a Zener-like tunneling between quasidegenerate vibrational eigenstates [8]. In this model, the tunneling strength depends on the offdiagonal elements of the phonon velocity operator, whereas Peierls's BTE considers only diagonal elements. This wave-like transport mechanism explains the temperature-enhanced thermal conductivity and its eventual saturation in amorphous solids [10,11]. A recent breakthrough is the development of a generalized WTE framework, which unifies these approaches by simultaneously addressing particlelike phonon propagating (population) and wavelike tunneling (coherence) [9]. This framework effectively captures both the effects of anharmonicity and disorder, providing a more holistic understanding of heat transport in crystalline materials with structural disorder.

The relative strength of propagating and tunneling transport mechanisms is determined by the interplay between phonon interband spacing, $\Delta \omega = |\omega(\mathbf{q})_s - \omega(\mathbf{q})_{s'}|$, and linewidth difference, $\Delta\Gamma = [\Gamma(\mathbf{q})_s + \Gamma(\mathbf{q})_{s'}]$. Here, $\omega(\mathbf{q})_s$ represents the frequency of a vibrational mode s at the wave vector \mathbf{q} , and $s \neq s'$. In simple crystalline materials (simple crystals) where $\Delta\omega \gg \frac{1}{2}\Delta\Gamma$, atomic vibrations are well described by particlelike phonons, and the thermal conductivity described by WTE is consistent with BTE predictions. Conversely, in amorphous materials characterized by strong structural disorder where $\Delta\omega \ll \frac{1}{2}\Delta\Gamma$, the wavelike tunneling transport becomes the primary heat transfer mechanism. Recently, Simoncelli et al.introduced the concept of "propagating-tunneling-invariant" (PTI) thermal conductivity, identifying materials where both mechanisms contribute nearly equally to thermal transport, resulting in temperature-independent thermal conductivity [12]. This discovery suggests a materials design principle: Introducing an optimal degree of structural disorder in weakly anharmonic materials can balance particlelike and wavelike transport

^{*}These authors contributed equally to this work.

[†]Contact author: liushi@westlake.edu.cn

mechanisms, thereby maintaining stable thermal conductivity across a broad temperature range.

In this work, we demonstrate intrinsic PTI thermal conductivity in crystalline materials with simple chemical compositions, without fine-tuning structural disorder. Our model system is monolayer β' -In₂Se₃ featuring in-plane ferroelectricity [13–16]. We find that this two-dimensional (2D) ferroelectric displays pronounced temperature-driven order-disorder behavior at temperatures well below the Curie temperature (T_c) . The thermally induced dipolar disorder generates strong intrinsic lattice anharmonicity, even in the absence of extrinsic structural defects. Importantly, the balanced compensation between wavelike tunneling and particlelike propagating results in an ultralow in-plane thermal conductivity of $\kappa \approx 0.6$ W/mK, which remains stable across a broad temperature range from 150 to 800 K. In contrast, the ferroelectric α -In₂Se₃ monolayer [13,17–20], which shares the same chemical composition as the β' phase, exhibits conventional $\kappa(T) \propto T^{-1}$ behavior. By suppressing dipolar disorder, an external electric field enables tunable anharmonicity and control over the $\kappa(T)$ scaling in β' -In₂Se₃. The α/β' phase boundary can also be reversibly driven by an in-plane field, achieving nonvolatile thermal switching with a ratio above 3.

II. COMPUTATIONAL METHODS

We calculate the thermal conductivity with both the WTE theory and classical molecular dynamics (MD) simulations. The key quantities in the WTE framework are the second-order and third-order interatomic force constants (IFCs), which can be obtained through the finite displacement method implemented in PHONO3PY [9,21–24], utilizing atomic forces computed with density functional theory (DFT). However, the computational cost becomes demanding for crystals with low symmetry. To address this challenge, we develop a machine learning force field, known as a neuroevolution potential (NEP) [25–27], for monolayer In₂Se₃.

A. Neuroevolution potential

The NEP model features an input layer of descriptors representing local atomic environments, constructed from Chebyshev and Legendre polynomials. It includes a single hidden layer with 80 tanh-activated neurons, trained via the separable natural evolution strategy. The training database comprises 21 955 monolayer configurations and 2808 bulk structures of various phases of In₂Se₃, with the energies and atomic forces computed using the projector augmented-wave formalism of DFT [28] implemented in VASP [29,30]. We choose the Perdew-Burke-Ernzerhof (PBE) functional as the exchange-correlation functional [31], a kinetic energy cutoff of 700 eV, and a k-point grid density of 0.3 Å^{-1} (equivalent to a $4 \times 4 \times 1$ k-point mesh for a 20-atom slab model). The rootmean-square errors (RMSEs) for training is 0.012 eV/atom for energy and 0.147 eV/Å for atomic forces [Figs. 1(a) and 1(b)]. The NEP model accurately reproduces the DFT phonon spectrum of monolayer α -In₂Se₃ [Fig. 1(c)].

To further test the accuracy of the NEP model, we carried out *ab initio* molecular dynamics (AIMD) simulations for

monolayer $\beta'\text{-In}_2Se_3$ at 300 K for several picoseconds using a 4×2 supercell containing 80 atoms. The NEP model was then used to evaluate the energies of configurations sampled along the AIMD trajectories. As shown in Fig. 1(d), the energy evolution obtained from the NEP closely follows that of the AIMD simulation, with a Pearson correlation coefficient of 0.95. This demonstrates the NEP model's accuracy in predicting energies for configurations sampled at finite temperatures that are not part of the training dataset. The results of additional validation tests are presented in Supplemental Material Sec. I [32].

B. Thermal transport calculations

The temperature-dependent WTE thermal conductivity of α - and β' -In₂Se₃ monolayers, computed using NEP-derived IFCs (Fig. 2), aligns well with values obtained from DFTderived IFCs employing a $6 \times 6 \times 1$ supercell and a 60×1 60×1 q-point grid. This provides strong evidence that the NEP model reliably reproduces higher-order derivatives of the potential energy surface that are critical for describing heat transport. In this study, we also estimate the heat conductivity via the homogeneous nonequilibrium molecular dynamics (HNEMD) [33,34] method based on the NEP model, which, in principle, captures all phonon-phonon interactions. All MD simulations are performed using the GPUMD package [26,35] with a time step of 1 fs. At each target temperature, the system is first equilibrated in the isothermal-isobaric (NPT) ensemble for at least 1 ns, followed by 10 ns of HNEMD runs in the canonical (NVT) ensemble employing a driving force parameter of 5×10^{-5} . We have prepared an online notebook to make public our training database, force field model, and training metadata [36].

C. Temperature-driven phase transitions

We report the temperature-driven α -to- β phase transition in monolayer In₂Se₃ from MD simulations using the NEP model. The MD trajectories are propagated using the velocity Verlet algorithm and a time step of 1 fs, with temperature and pressure controlled by a Berendsen barostat, respectively, as implemented in GPUMD [26,35]. At each temperature, the production run is 1 ns to ensure enough sampling to obtain statistically reliable values of thermodynamics properties. Consistent with our earlier study [37], we use the out-of-plane displacement (D_z) of the central Se atoms relative to the geometric center of the monolayer as an indicator of local symmetry breaking [Fig. 3(b)]. Figure 3(a) illustrates the evolution of D_z with increasing temperature, revealing a ferroelectric-to-paraelectric $(\alpha$ -to- $\beta)$ phase transition at 550 K, with snapshots at 300 and 650 K shown in Fig. 3(c). These results further confirm the accuracy of the NEP model in simulating the finite-temperature properties of monolayer In₂Se₃.

III. RESULTS AND DISCUSSION

A. Thermal conductivity of monolayer α-In₂Se₃

Indium selenides represent a versatile class of materials that supports various stoichiometric ratios and has been

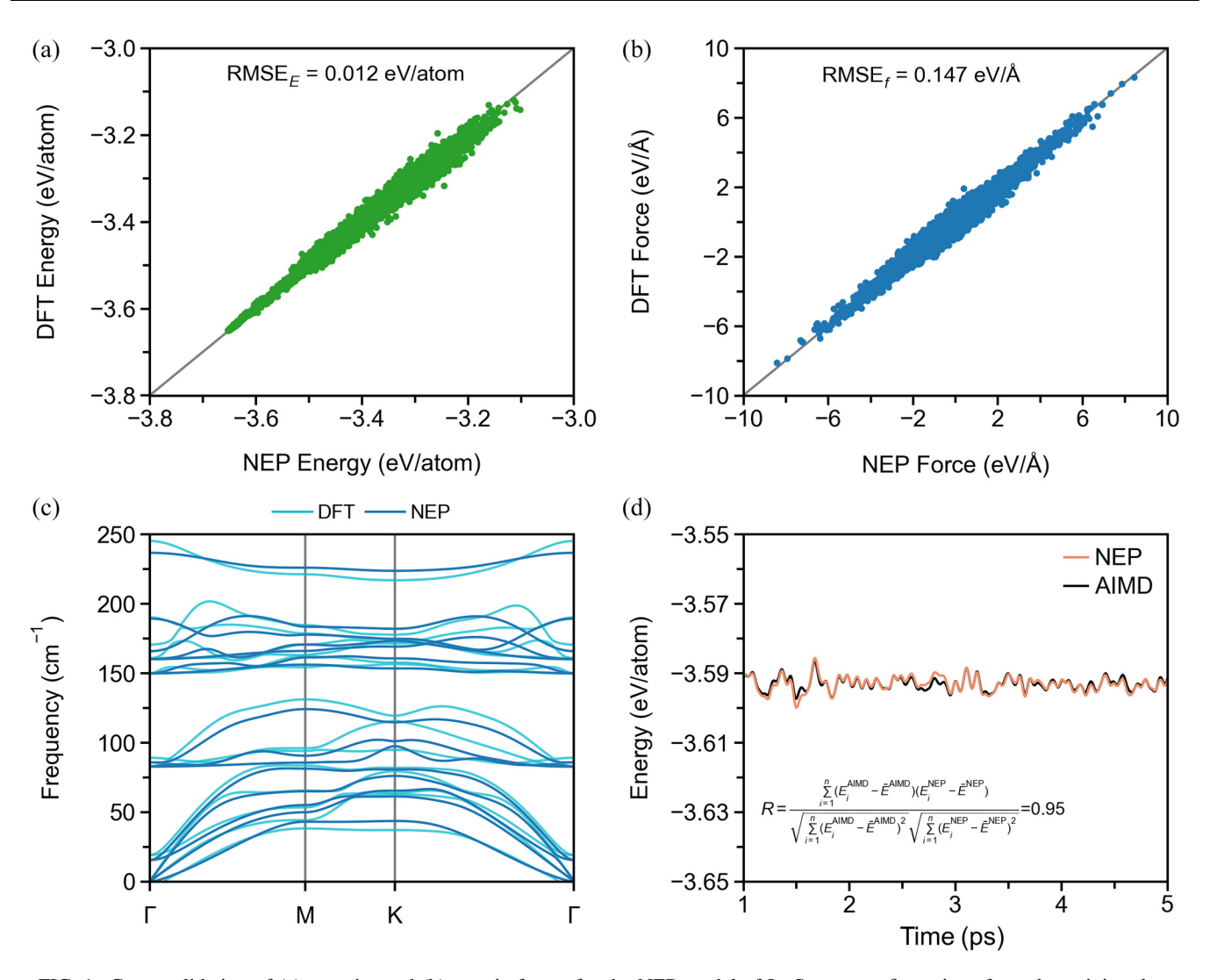


FIG. 1. Cross-validation of (a) energies and (b) atomic forces for the NEP model of In_2Se_3 on configurations from the training dataset. (c) Phonon dispersion relations of monolayer α - In_2Se_3 computed using DFT and NEP. (d) Energies of configurations sampled by AIMD for the β' monolayer at 300 K, validated using the NEP model.

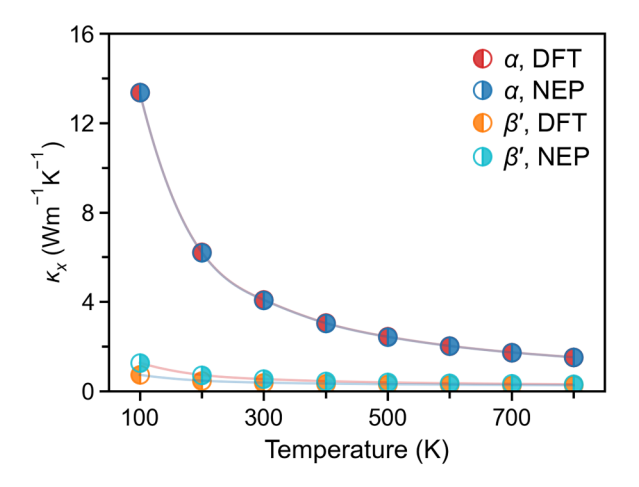


FIG. 2. Comparison of the temperature-dependent thermal conductivity of monolayer α - and β' -In₂Se₃, calculated using second-order and third-order interatomic force constants obtained from DFT and the NEP model, respectively.

extensively studied for thermoelectric applications [38–40]. Recently, quasi-two-dimensional α - and β' -In₂Se₃ have garnered significant attention due to the room-temperature ferroic properties, even at the monolayer limit [37,38,41]. Specifically, monolayer In₂Se₃ comprises a covalently bonded Se-In-Se-In-Se quintuple layer, with the central Se atoms displaced out of plane in the α phase [Fig. 4(a)] and in plane in the β' phase [Fig. 4(b)]. At elevated temperatures, both polar phases transition into the nonpolar β phase [Fig. 4(c)]. We calculate the in-plane thermal conductivity (κ_x) along the x direction for monolayer α-In₂Se₃ using both the WTE theory $(\kappa_{\rm WTE})$ and HNEMD $(\kappa_{\rm MD})$. The calculations of $\kappa_{\rm WTE}$ account for three-phonon scattering, based on second- and third-order IFCs derived from the NEP model. As shown in Fig. 4(d), for the α phase, both $\kappa_{\rm WTE}$ and $\kappa_{\rm MD}$ display a T^{-1} dependence on temperature, characteristic of simple crystals. The values of $\kappa_{\rm WTE}$ computed using NEP-derived IFCs also agree closely with previously reported DFT values [41,42]. As expected, $\kappa_{\rm MD}$ is slightly lower than $\kappa_{\rm WTE}$, as MD simulations capture all orders of phonon scattering processes.

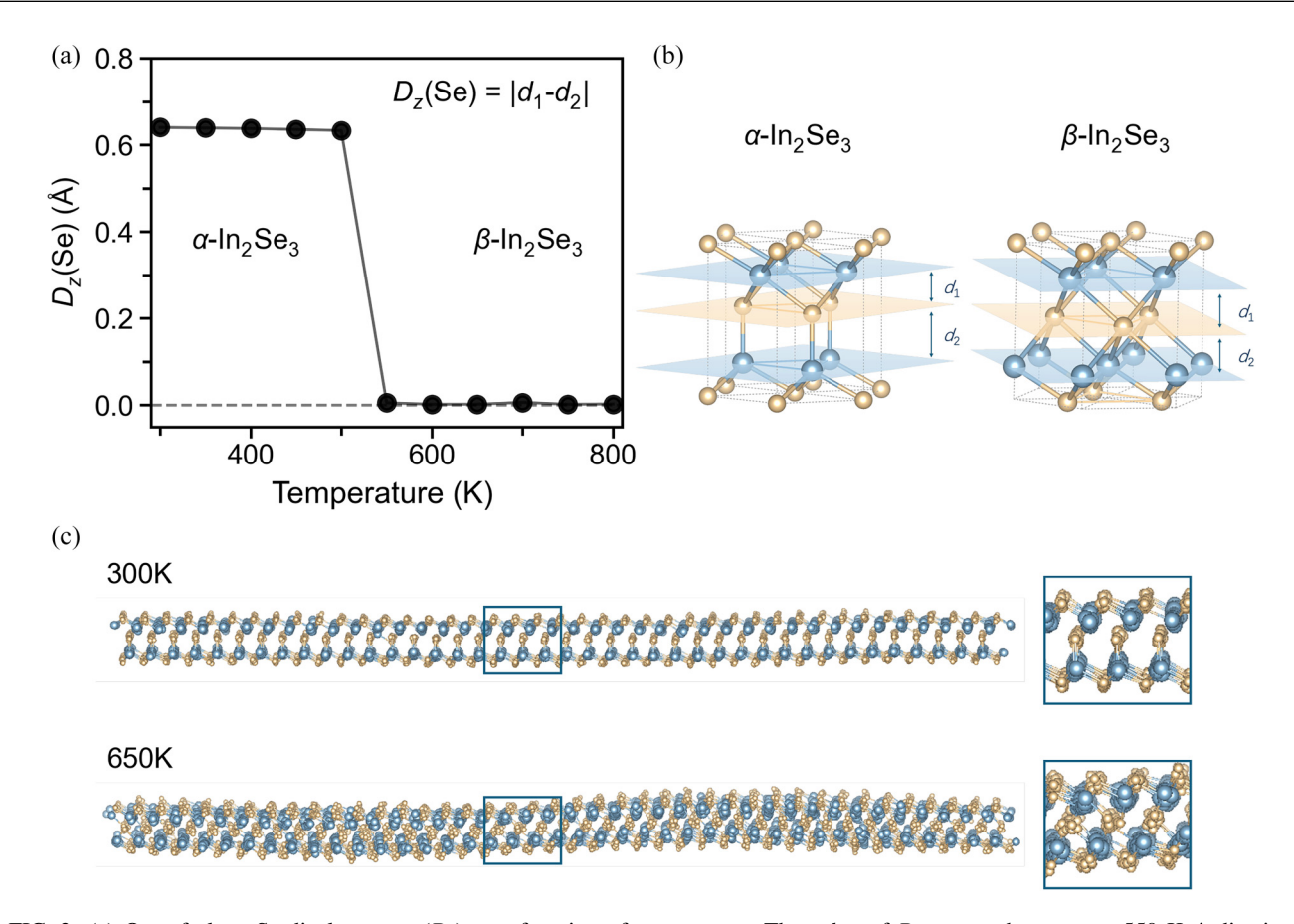


FIG. 3. (a) Out-of-plane Se displacement (D_z) as a function of temperature. The value of D_z approaches zero at 550 K, indicating an $\alpha \to \beta$ phase transition [37]. (b) Schematic illustrations of the crystal structures of monolayer α - and β -In₂Se₃. Snapshots of the monolayer configuration from MD simulations at (c) 300 and 650 K.

As shown in Fig. 3, our MD simulations reproduce the experimentally observed temperature-driven transition from the ferroelectric α phase to the paraelectric β phase [43]. This transition is accompanied by a drop in κ_{MD} to $0.58~{\rm W\,m^{-1}\,K^{-1}}$ above $T_c \approx 600~{\rm K}$. In contrast, the WTE theory, which considers only thermal effects on phonon occupations and neglects structural transitions, predicts a smooth decrease in $\kappa_{\rm WTE}$ beyond T_c . To gain further insight, we decompose κ_{WTE} into contributions from phonon population (κ_p) and coherence (κ_c) . The analysis shows $\kappa_{\rm WTE} \approx \kappa_{\rm p}$, with negligible $\kappa_{\rm c}$, indicating strongly harmonic bonding and dominant particlelike phonon transport in α -In₂Se₃. We further assess four-phonon scattering effects by computing $\kappa_{p,3ph+4ph}$ using fourth-order IFCs derived from the NEP model. As shown in Fig. 4(d), these values align closely with MD results in the α phase, highlighting the importance of higher-order anharmonicity.

B. Temperature-invariant ultralow thermal conductivity of monolayer β' -In₂Se₃

Despite sharing the same chemical composition, the β' -In₂Se₃ monolayer exhibits significantly lower thermal conductivity and a more complicated temperature dependence [Fig. 4(e)] compared to the α phase. At T=50 K, the values of $\kappa_{\rm WTE}$ and $\kappa_{\rm MD}$ show good agreement, both around 1.25 W m⁻¹ K⁻¹. This is at least an order of magnitude

lower than the thermal conductivity of the α phase, which is $33.7 \text{ W m}^{-1} \text{ K}^{-1}$ at the same temperature. Phonon lifetime calculations show that the α phase has significantly longer lifetimes than the β' phase, mainly due to its reduced scattering phase space (Fig. S10). As the temperature rises, κ_{WTF} decays much more slowly than the typical T^{-1} scaling. As illustrated in Fig. 4(e), while the particlelike contribution κ_p adheres to the T^{-1} dependence, the coherence contribution κ_c becomes increasingly significant for T > 50 K. For example, at T = 100 K, κ_c reaches 0.086 W m⁻¹ K⁻¹, accounting for approximately 12% of the total thermal conductivity of 0.725 W m⁻¹ K⁻¹. The onset of a wavelike transport mechanism at such a low temperature is unusual and points to a strongly anharmonic lattice in the β' -In₂Se₃ monolayer. Importantly, the compensating variations of κ_p and κ_c realize the PTI thermal conductivity, where $\kappa_{\rm WTE}$ remains around 0.34 W m⁻¹ K⁻¹ with a standard deviation (σ_{κ}) of 0.08 W m⁻¹ K⁻¹ for temperatures above 150 K.

Consistent with WTE calculations, MD simulations also predict the emergence of temperature-invariant thermal conductivity in the β' -In₂Se₃ monolayer. Notably, κ_{MD} remains nearly constant across the $\beta' \to \beta$ phase transition, stabilizing at $\approx 0.60 \text{ W m}^{-1} \text{ K}^{-1}$ ($\sigma_{\kappa} = 0.07 \text{ W m}^{-1} \text{ K}^{-1}$) from 150 to 800 K. Such temperature-invariant heat conductivity over a broad temperature range underscores the unique thermal transport properties of the β' -In₂Se₃ monolayer. We find that κ_{MD} values are consistently higher than those predicted by

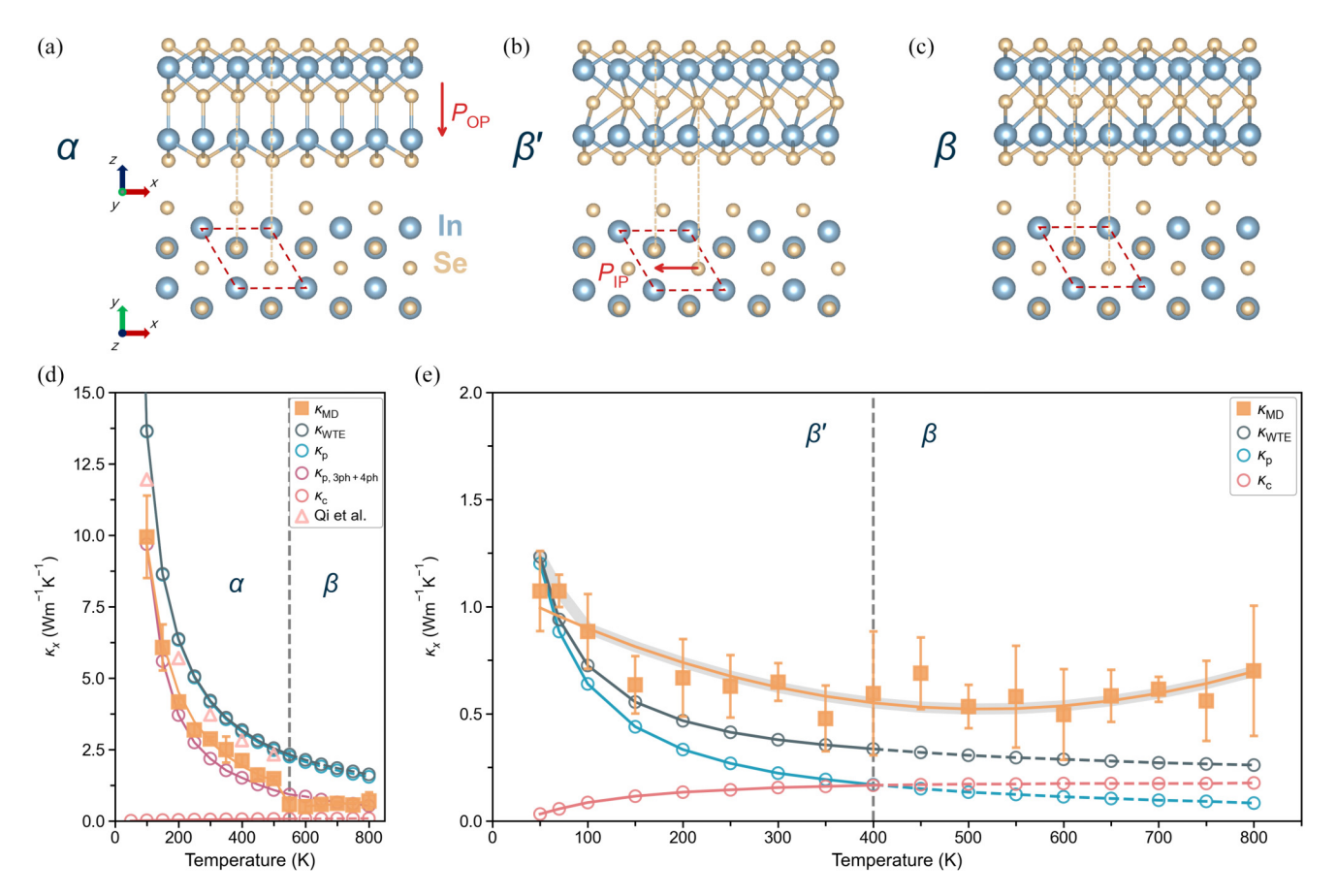


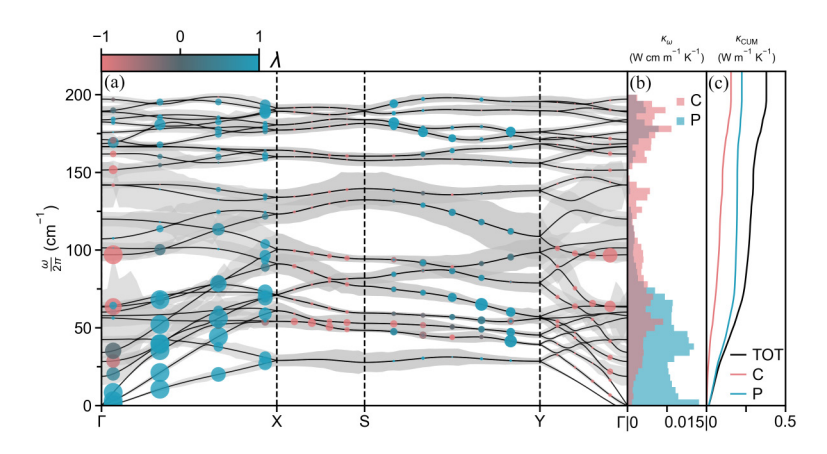
FIG. 4. Temperature dependent thermal conductivity of monolayer In_2Se_3 . Schematics of crystal structures of monolayer In_2Se_3 in the (a) α , (b) β' , and (c) β phases. The red arrow represents the direction of local polarization. (d) Thermal conductivity of the α phase as a function of temperature, calculated using the WTE method (κ_{WTE} , open circles) and the HNEMD method (κ_{MD} , solid squares). The κ_{WTE} is decomposed into the particlelike propagating (population) contribution (κ_p) and wavelike tunneling (coherence) contribution (κ_c). Since the WTE method does not capture the phase transition, the values of κ_{WTE} beyond $T_c \approx 550$ K (vertical gray line) are connected by a dashed line. (e) Thermal conductivity of the β' phase as a function of temperature. The vertical gray line marks the transition from the β' phase to the β phase at 400 K.

 $\kappa_{\rm WTE}$. Similar discrepancies have been reported for other low-thermal-conductivity materials, such as MgSiO₄, where $\kappa_{\rm MD}$ exceeds BTE-based predictions [44,45]. Our detailed analysis shows that, in the single-domain limit, using second-and third-order IFCs extracted from temperature-dependent effective potentials yield WTE values higher than MD results, aligning with the conventional understanding that MD captures full-order anharmonicity at finite temperatures (see Supplemental Material Sec. III [32]). Despite the quantitative differences, the near temperature invariance of both $\kappa_{\rm WTE}$ and $\kappa_{\rm MD}$ in the β' phase [Fig. 4(e)] demonstrates that WTE captures the correct qualitative trend.

C. WTE mode analysis

The presence of PTI thermal conductivity in the β' -In₂Se₃ monolayer is corroborated through an analysis of phonon properties at 300 K. The phonon spectrum [Fig. 5(a)] with shaded gray areas representing half the phonon linewidth $[\Gamma(\mathbf{q})_s/2]$ at 300 K, reveals low-energy flat branches with overlapping linewidths. For a given phonon eigenstate (\mathbf{q}, s) , we define the parameter $\lambda = \frac{\kappa_p - \kappa_c}{\kappa_p + \kappa_c}$. Phonons with large group velocities and low anharmonicity, characterized by

small $\Gamma(\mathbf{q})_s$, predominantly contribute to the particlelike term $(\lambda \to 1)$. In contrast, highly anharmonic flat bands with large $\Gamma(\mathbf{q})_s$ primarily contribute to the coherence term $(\lambda \to -1)$. The thermal conductivity density of states [Fig. 5(b)] shows that κ_p is dominated by low-frequency phonons below 75 cm⁻¹. However, the cumulative contributions from phonons across a broad frequency range make the coherence mechanism significant, accounting for approximately 40% of the total conductivity [Fig. 5(c)]. The role of phonon coherence is further elucidated by comparing the three-phonon lifetime (τ_{3ph}) to two critical limits: the Wigner limit, given by $\tau_{W}=$ $3N/\omega_{\rm max}$, and the Ioffe-Regel limit, defined as $\tau_{\rm IR}=\omega^{-1}$ [46–49]. Here, ω_{max} represents the maximum phonon frequency, and N is the number of atoms in the primitive cell. As shown in Fig. 5(d), a substantial number of phonons fall between the Wigner limit and the Ioffe-Regel limit, indicating that phonons are in a transitional regime, neither fully particlelike nor entirely localized. This transitional behavior explains the significant influence of phonon coherence on the thermal conductivity of β' -In₂Se₃ at 300 K. Figure S11 shows the temperature-dependent evolution of the relative contributions from propagating and tunneling terms, revealing that they contribute equally at 400 K.



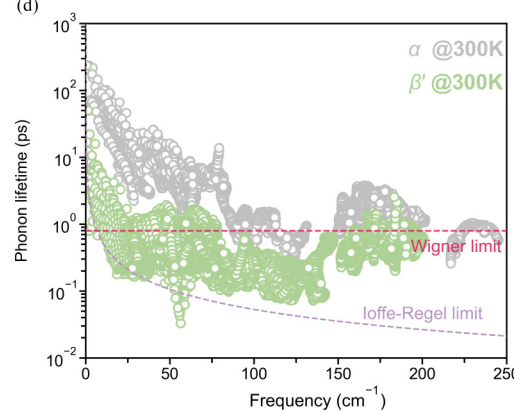


FIG. 5. Phonon properties and heat conduction mechanisms in monolayer β' -In₂Se₃ at 300 K. (a) Phonon spectrum of the β' phase with shared gray areas representing half the phonon linewidths $[\Gamma(\mathbf{q})_s/2$ for graphical clarity] at 300 K. The origin and contribution of thermal conductivity for representative phonon eigenstates are analyzed using the parameter $\lambda = \frac{\kappa_p - \kappa_c}{\kappa_p + \kappa_c}$. The size of colored circles scales with the total thermal conductivity and the color indicates the dominant contribution, blue for the particlelike population mechanism and red for the wavelike coherence mechanism. (b) Thermal conductivity density of states (κ_ω) decomposed into contributions from the population mechanism (P, blue) and the coherence mechanism (C, red). (c) Cumulative total thermal conductivity $(\kappa_{\text{CUM}}, \text{black})$ as the sum of the population contribution and coherence contribution. (d) Three-phonon lifetimes as a function of phonon frequency at 300 K, shown for the α phase (gray) and the β' phase (green). The dashed red line represents the Wigner limit, while the dashed purple line marks the Ioffe-Regel limit.

D. Dipolar disorder from MD

The WTE thermal conductivity exhibits the onset of PTI behavior at a low temperature of \approx 150 K, indicating strong lattice anharmonicity in monolayer β' -In₂Se₃ even under weak thermal fluctuations. This behavior can be attributed to the intrinsic sombrero-shaped potential energy surface (PES; see both PBE and SCAN0 results in Fig. S6). Unit-cell DFT calculations reveal a competing polar phase with in-plane polarization, belonging to the C2 space group, which we designate as β'' . Both β' and β'' originate from unstable zone-center phonon modes of the nonpolar β phase [Fig. 6(a)] [13,15,50]. The two phases differ in the direction of centrallayer Se atom displacements: In β' , Se atoms shift toward the midpoint between two neighboring In atoms, while in β'' , they point directly toward a single In atom [Fig. 6(b)]. Notably, the β'' phase is only 1.2 meV/atom higher in energy than β' , suggesting a shallow PES and enhanced anharmonicity.

The sombrero-shaped PES at finite temperatures manifests in the formation of complex domain structures. To probe this behavior, we analyze the orientations (θ) and magnitudes (ρ) of local Se displacements in the central layer, using 1000 instantaneous configurations sampled uniformly over a 100 ps MD simulation. This statistical approach captures the dynamic structure at a given temperature. To quantify symmetry, we evaluate $\Omega(\theta)\langle \rho(\theta)\rangle$, where $\Omega(\theta)$ is the probability density of Se displacements with in-plane angle θ , and $\langle \rho(\theta) \rangle$ is their average magnitude. As shown in the polar plots in Fig. 6(c), the butterfly-shaped distribution at 200 K reveals six preferred orientations: four associated with the β'' phase (peaks at $\pi/3$, $2\pi/3$, $4\pi/3$, and $5\pi/3$) and two with the β' phase (peaks at $\pi/2$ and $3\pi/2$). This pattern corresponds to nanoscale antiferroelectric domains, as illustrated in the MD snapshot [top panel of Fig. 6(d)]. These results align with previous observations of nanostriped antiferroelectric ordering in β' -In₂Se₃, confirmed by real-space imaging and

polarization mapping via scanning transmission electron microscopy [15,51]. At 300 K, the distribution becomes more isotropic, with two broad peaks near $\pi/2$ and $3\pi/2$, and a reduced $\langle \rho(\theta) \rangle$, indicating weaker local polar order. By 400 K, the Se displacements in the β phase are nearly orientation independent, with uniform $\Omega(\theta)$ across all angles. Despite this isotropy, most central-layer Se atoms remain locally displaced [Fig. 6(d), bottom], highlighting the order-disorder nature of the $\beta' \to \beta$ phase transition. This dynamic disorder of Se atoms, which arises from a shallow sombrero-shaped PES, is fundamentally different from that caused by ion diffusion in superionic conductors [52], where entire cations or anions become mobile and undergo long-range diffusion throughout the crystal.

E. Electric-field-driven tunable thermal conductivity

We find that the degree of anharmonicity in monolayer β' -In₂Se₃ can be effectively modulated by external electric fields. Experimentally, a transistorlike device setup has been used to apply in-plane electric fields to α-In₂Se₃ connecting the source and drain [53]. Figure 7(a) shows the temperature dependence of κ_x under an electric field applied along the x axis, for varying field strengths. The values of κ_x are computed using equilibrium finite-field MD simulations combined with the Kubo formula (see κ_x convergence tests in Fig. S5), with the electric field effect treated using the "force method" [54,55]. Our results show that κ_x increases with electric field strength at fixed temperature. At 4 MV/cm, κ_x exhibits pronounced temperature dependence [solid line in Fig. 7(a)], indicating a resurgence of particlelike transport. $\kappa(T)$ approximately follows a T^{-1} dependence between 150 and 500 K (see Supplemental Material Sec. II [32]). However, at certain temperatures (e.g., 100 K), the upper limit of the error bar for 0 MV/cm overlaps with the lower limit for 4 MV/cm. This is primarily due to the intrinsically low thermal conductivity

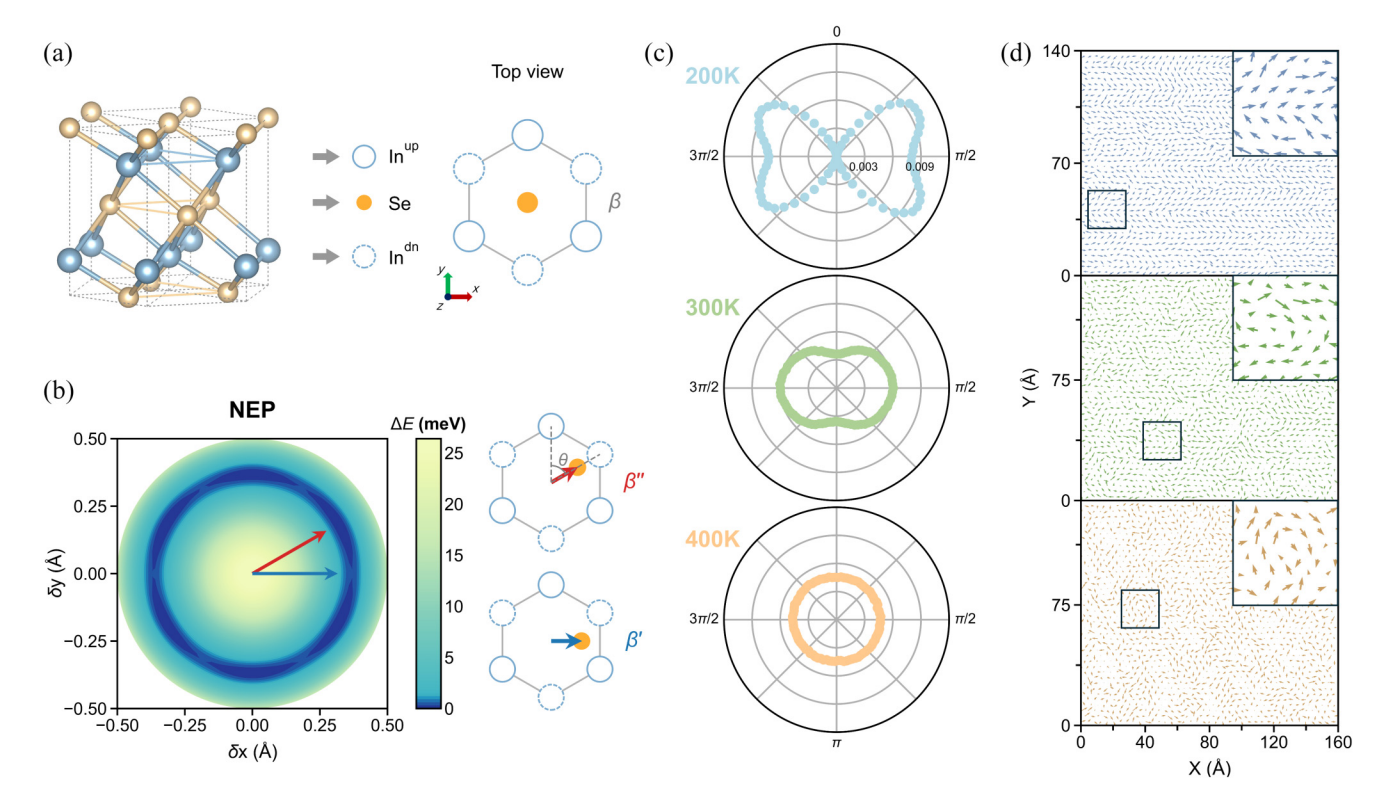


FIG. 6. Dipolar disorder originated from a sombrero-shaped potential energy surface. (a) Schematic illustrations of side view and top view of the paraelectric β phase. For clarity, the top view does not display the outermost Se atoms. (b) Calculated potential energy surface by displacing the central Se atom in the β -In₂Se₃ unit cell. The red arrow indicates the Se atom shift toward the hexagon corner, characteristic of the β'' phase, while the blue arrow represents the Se atom shift toward the hexagon edge, characteristic of the β' phase. (c) Temperature dependence of $\Omega(\theta)\langle \rho(\theta)\rangle$, where $\Omega(\theta)$ is the probability density for Se displacements at angle θ and $\langle \rho(\theta)\rangle$ is the average magnitude of Se displacements for the same orientation. (d) Snapshots from MD simulations. Each arrow represents the local Se displacement in an 8000-atom supercell, with an enlarged view provided in the top-right corner.

at these temperatures, which results in larger relative uncertainties. Although we performed multiple independent MD simulations to reduce statistical noise, this overlap persists. Therefore, the thermal switching ratio should be interpreted

as semiquantitative. The phonon density of states obtained from MD trajectories confirm that the electric field promotes the density of high-frequency phonons. At 150 K, the heat conductivity switching ratio, defined as the ratio of κ_x in the

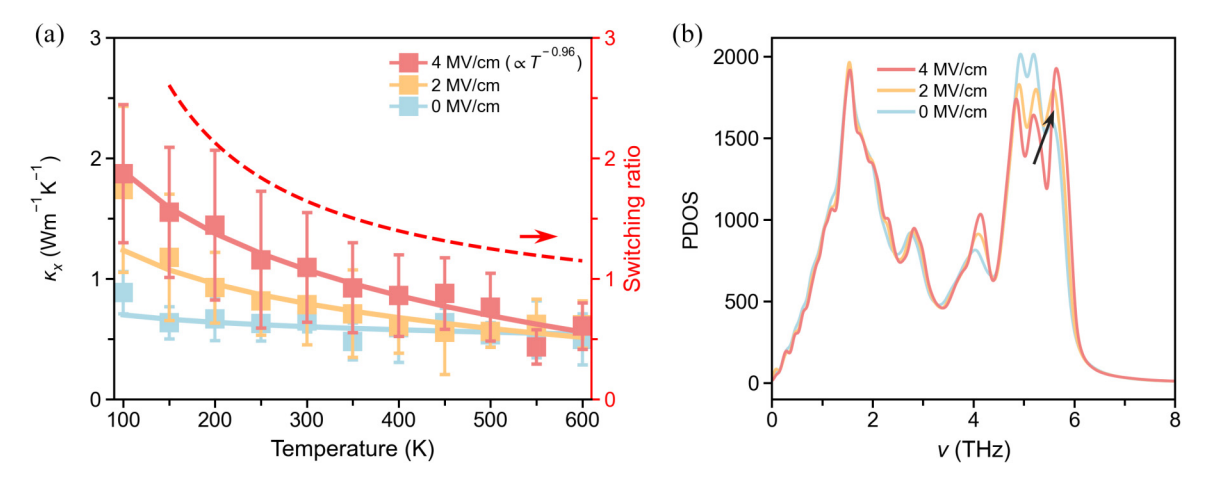


FIG. 7. Electric-field-tunable temperature dependence of in-plane thermal conductivity in the β' -In₂Se₃ monolayer. (a) Temperature dependence of κ_x under electric fields applied along the x axis. The red solid line represents a fit of $\kappa(T) \propto T^{-1}$ using data between 150 and 500 K. The red dashed line is the heat conductivity switching ratio at 4 MV/cm. (b) Phonon density of states (PDOS) at 200 K for various electric field strengths. The arrow highlights the promotion of the high-frequency phonons.

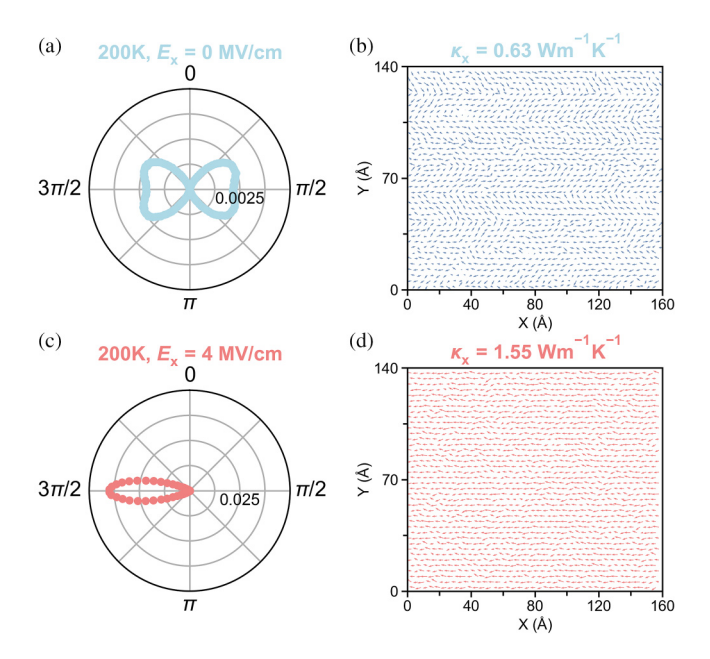


FIG. 8. (a) Angular distribution $\Omega(\theta)\langle\rho(\theta)\rangle$ and (b) snapshot from MD simulations at 200 K. Each arrow in (d) represents the local Se displacement in an 8000-atom supercell. (c) $\Omega(\theta)\langle\rho(\theta)\rangle$ and (d) snapshot from MD simulations under an in-plane electric field of 4 MV/cm at 200 K.

high-conductivity state to its value in the low-conductivity state, reaches a large value of ≈ 2.5 [see the dashed line in Fig. 7(a)].

Figure 8 compares the dipole distribution before and after applying an electric field at 200 K. The energy barrier between the β' and β'' in-plane polarization states is exceptionally low ($\Delta E \approx 0.077$ meV/atom for PBE and 0.166 meV/atom for

SCAN0 in Fig. S6), enabling significant dipolar fluctuations even at modest temperatures. Therefore, even at a relatively low temperature of 200 K, the thermal energy ($k_BT \approx 17.2$ meV/atom) allows frequent transitions between polarization variants. These dynamic fluctuations manifest in the broad angular distributions in $\Omega(\theta)\langle \rho(\theta)\rangle$ [Fig. 8(a)] and the complex domain structures with dense domain walls [Fig. 8(b)]. Furthermore, applying an in-plane electric field suppresses dipolar disorder by aligning local dipoles. This field-induced ordering lifts the degeneracy of the sombrero-shaped PES, collapsing it into a single-well configuration. As shown in Fig. 8(c), the butterfly-shaped distribution transforms into an elliptical profile aligned with the field. The spatial dipole distribution in Fig. 8(d) confirms the emergence of long-range in-plane dipolar order in the β' monolayer. Finally, we find that an electric field can reversibly drive the motion of the α/β' phase boundary (Fig. 9), enabling nonvolatile control over the relative fraction of the high-conductivity α phase and the low-conductivity β' phase, with an estimated switching ratio exceeding 3.0.

IV. CONCLUSIONS

In summary, the intrinsic propagating-tunneling-invariant thermal conductivity observed in ferroelectric monolayer β' -In₂Se₃ demonstrates that dipolar dynamics in two dimensions can be harnessed to engineer lattice anharmonicity and achieve unconventional thermal transport behavior in materials with simple chemical compositions. The coexistence and compensation of particlelike and wavelike heat transport mechanisms, driven by the strong order-disorder behavior of dipoles arising from the sombrero-shaped energy landscape, establish a design principle for realizing temperature-invariant thermal conductivity in crystalline systems, without relying

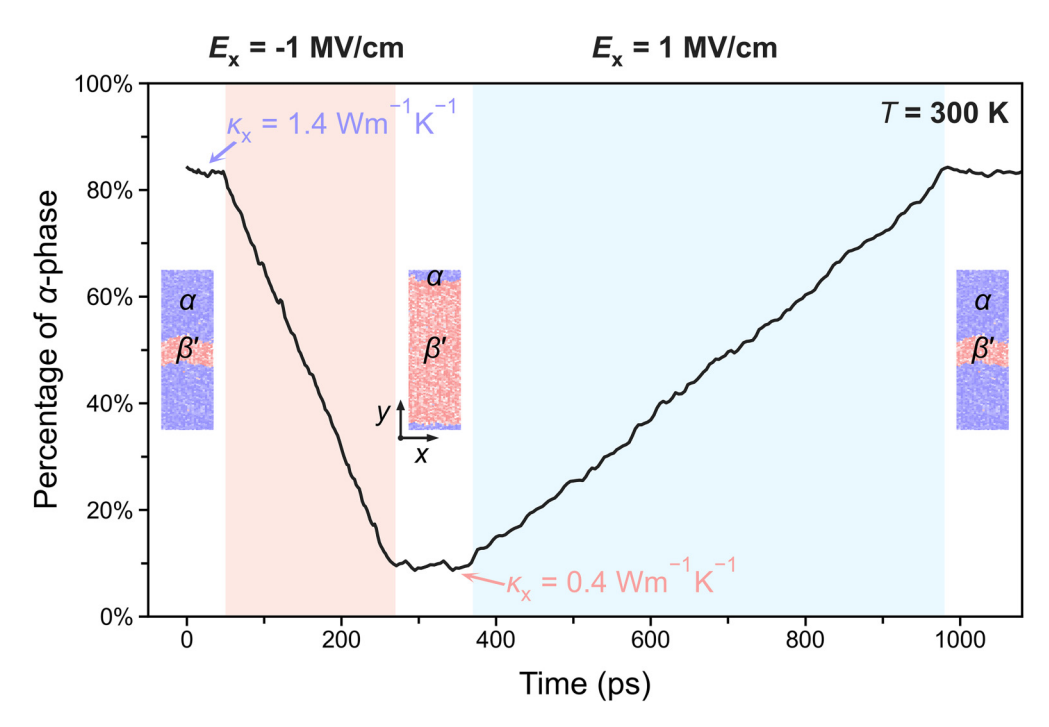


FIG. 9. Electric-field-driven motion of the $\alpha-\beta'$ phase boundary. The ratio between the α and β' phases in the monolayer can be reversibly tuned.

on extrinsic structural modifications or defects. This discovery challenges the conventional paradigms of thermal transport in solids by revealing how intrinsic anharmonic effects, induced by ferroelectric dipolar fluctuations, can dominate heat conduction even at relatively low temperatures. The tunability of thermal transport via external electric fields further underscores the potential of β' -In₂Se₃ for thermal management and adaptive solid-state reconfigurable thermal components such as thermal dipoles [56,57], transistors [56,58], and neurons [59], where precise control of heat flow is regulated by gate voltages. Beyond technological implications, it also serves a model system for exploring the fundamental physics of anharmonicity and phonon coherence in low-dimensional materials.

ACKNOWLEDGMENTS

This work acknowledges supports from Zhejiang Provincial Natural Science Foundation of China (Grant No. LR25A040004) and Natural Science Foundation of China (Grants No. 92370104 and No. 52002335). The computational resource is provided by Westlake HPC Center. The authors sincerely thank Dr. Zekun Chen for his advice on the details of the thermal conductivity calculations.

DATA AVAILABILITY

The data that support the findings of this article are openly available [36].

- [1] S. Lee, K. Hippalgaonkar, F. Yang, J. Hong, C. Ko, J. Suh, K. Liu, K. Wang, J. J. Urban, X. Zhang, C. Dames, S. A. Hartnoll, O. Delaire, and J. Wu, Anomalously low electronic thermal conductivity in metallic vanadium dioxide, Science 355, 371 (2017).
- [2] W. Dai, L. Lv, T. Ma, X. Wang, J. Ying, Q. Yan, X. Tan, J. Gao, C. Xue, J. Yu, Y. Yao, Q. Wei, R. Sun, Y. Wang, T. Liu, T. Chen, R. Xiang, N. Jiang, Q. Xue, C. Wong *et al.*, Multiscale structural modulation of anisotropic graphene framework for polymer composites achieving highly efficient thermal energy management, Adv. Sci. 8, 2003734 (2021).
- [3] Z. He, Y. Yan, and Z. Zhang, Thermal management and temperature uniformity enhancement of electronic devices by micro heat sinks: A review, Energy **216**, 119223 (2021).
- [4] X. Qian, J. Zhou, and G. Chen, Phonon-engineered extreme thermal conductivity materials, Nat. Mater. 20, 1188 (2021).
- [5] Q. Yan and M. G. Kanatzidis, High-performance thermoelectrics and challenges for practical devices, Nat. Mater. 21, 503 (2021).
- [6] B. Jiang, Y. Yu, J. Cui, X. Liu, L. Xie, J. Liao, Q. Zhang, Y. Huang, S. Ning, B. Jia, B. Zhu, S. Bai, L. Chen, S. J. Pennycook, and J. He, High-entropy-stabilized chalcogenides with high thermoelectric performance, Science 371, 830 (2021).
- [7] R. Peierls, Zur kinetischen theorie der wärmeleitung in kristallen, Ann. Phys. (NY) **395**, 1055 (1929).
- [8] P. B. Allen and J. L. Feldman, Thermal conductivity of glasses: Theory and application to amorphous Si, Phys. Rev. Lett. 62, 645 (1989).
- [9] M. Simoncelli, N. Marzari, and F. Mauri, Unified theory of thermal transport in crystals and glasses, Nat. Phys. 15, 809 (2019).
- [10] Z. Zhang, Y. Guo, M. Bescond, J. Chen, M. Nomura, and S. Volz, How coherence is governing diffuson heat transfer in amorphous solids, npj Comput. Mater. 8, 96 (2022).
- [11] L. Yang and B.-Y. Cao, Significant anharmonicity of thermal transport in amorphous silica at high temperature, Phys. Status Solidi RRL 16, 2200217 (2022).
- [12] M. Simoncelli, D. Fournier, M. Marangolo et al., Temperature-invariant heat conductivity from compensating crystalline and glassy transport: From the Steinbach meteorite to furnace bricks, Research Square (2024), doi:10.21203/rs.3.rs-4456620/v1.

- [13] W. Ding, J. Zhu, Z. Wang, Y. Gao, D. Xiao, Y. Gu, Z. Zhang, and W. Zhu, Prediction of intrinsic two-dimensional ferroelectrics in In₂Se₃ and other III₂-VI₃ van der Waals materials, Nat. Commun. **8**, 14956 (2017).
- [14] C. Zheng, L. Yu, L. Zhu, J. L. Collins, D. Kim, Y. Lou, C. Xu, M. Li, Z. Wei, Y. Zhang, M. T. Edmonds, S. Li, J. Seidel, Y. Zhu, J. Z. Liu, W.-X. Tang, and M. S. Fuhrer, Room temperature in-plane ferroelectricity in van der Waals In₂Se₃, Sci. Adv. 4, eaar7720 (2018).
- [15] Z. Zhang, J. Nie, Z. Zhang, Y. Yuan, Y. Fu, and W. Zhang, Atomic visualization and switching of ferroelectric order in β-In₂Se₃ films at the single layer limit, Adv. Mater. 34, 2106951 (2022).
- [16] F. Zhang, Z. Wang, J. Dong, A. Nie, J. Xiang, W. Zhu, Z. Liu, and C. Tao, Atomic-scale observation of reversible thermally driven phase transformation in 2D In₂Se₃, ACS Nano 13, 8004 (2019).
- [17] Y. Zhou, D. Wu, Y. Zhu, Y. Cho, Q. He, X. Yang, K. Herrera, Z. Chu, Y. Han, M. C. Downer, H. Peng, and K. Lai, Out-ofplane piezoelectricity and ferroelectricity in layered α-In₂Se₃ nanoflakes, Nano Lett. 17, 5508 (2017).
- [18] F. Xue, W. Hu, K.-C. Lee, L.-S. Lu, J. Zhang, H.-L. Tang, A. Han, W.-T. Hsu, S. Tu, W.-H. Chang, C.-H. Lien, J.-H. He, Z. Zhang, L.-J. Li, and X. Zhang, Room-temperature ferroelectricity in hexagonally layered α-In₂Se₃ nanoflakes down to the monolayer limit, Adv. Funct. Mater. 28, 1803738 (2018).
- [19] C. Cui, W.-J. Hu, X. Yan, C. Addiego, W. Gao, Y. Wang, Z. Wang, L. Li, Y. Cheng, P. Li, X. Zhang, H. N. Alshareef, T. Wu, W. Zhu, X. Pan, and L.-J. Li, Intercorrelated in-plane and out-of-plane ferroelectricity in ultrathin two-dimensional layered semiconductor In₂Se₃, Nano Lett. 18, 1253 (2018).
- [20] S. Wan, Y. Li, W. Li, X. Mao, W. Zhu, and H. Zeng, Room-temperature ferroelectricity and a switchable diode effect in two-dimensional α-In₂Se₃ thin layers, Nanoscale 10, 14885 (2018).
- [21] A. Togo, L. Chaput, and I. Tanaka, Distributions of phonon lifetimes in Brillouin zones, Phys. Rev. B 91, 094306 (2015).
- [22] A. Togo, L. Chaput, T. Tadano, and I. Tanaka, Implementation strategies in phonopy and phono3py, J. Phys.: Condens. Matter 35, 353001 (2023).
- [23] L. Chaput, Direct solution to the linearized phonon Boltzmann equation, Phys. Rev. Lett. **110**, 265506 (2013).

- [24] M. Simoncelli, N. Marzari, and F. Mauri, Wigner formulation of thermal transport in solids, Phys. Rev. X 12, 041011 (2022).
- [25] Z. Fan, Z. Zeng, C. Zhang, Y. Wang, K. Song, H. Dong, Y. Chen, and T. Ala-Nissila, Neuroevolution machine learning potentials: Combining high accuracy and low cost in atomistic simulations and application to heat transport, Phys. Rev. B 104, 104309 (2021).
- [26] Z. Fan, Y. Wang, P. Ying, K. Song, J. Wang, Y. Wang, Z. Zeng, K. Xu, E. Lindgren, J. M. Rahm, A. J. Gabourie, J. Liu, H. Dong, J. Wu, Y. Chen, Z. Zhong, J. Sun, P. Erhart, Y. Su, and T. Ala-Nissila, GPUMD: A package for constructing accurate machine-learned potentials and performing highly efficient atomistic simulations, J. Chem. Phys. 157, 114801 (2022).
- [27] S. Sonti, C. Sun, Z. Chen, R. M. Kowalski, J. S. Kowalski, D. Donadio, S.-H. Ahn, and A. R. Kulkarni, Stability and dynamics of zeolite-confined gold nanoclusters, J. Chem. Theory Comput. 20, 8261 (2024).
- [28] P. E. Blöchl, Projector augmented-wave method, Phys. Rev. B **50**, 17953 (1994).
- [29] G. Kresse and J. Furthmüller, Efficient iterative schemes for *ab initio* total-energy calculations using a plane-wave basis set, Phys. Rev. B **54**, 11169 (1996).
- [30] G. Kresse and J. Furthmüller, Efficiency of ab-initio total energy calculations for metals and semiconductors using a plane-wave basis set, Comput. Mater. Sci. 6, 15 (1996).
- [31] J. P. Perdew, A. Ruzsinszky, G. I. Csonka, O. A. Vydrov, G. E. Scuseria, L. A. Constantin, X. Zhou, and K. Burke, Restoring the density-gradient expansion for exchange in solids and surfaces, Phys. Rev. Lett. 100, 136406 (2008).
- [32] See Supplemental Material at http://link.aps.org/supplemental/ 10.1103/3nqr-9b32 for computation methods, NEP model validation, AIMD and HNEMD/EMD convergence, temperaturedependent thermal conductivity scaling, WTE-based moderesolved phonon transport analysis, and electric field modulation of lattice anharmonicity, which includes Refs. [33,34,37].
- [33] X. Wu and Q. Han, Transition from incoherent to coherent phonon thermal transport across graphene/h-BN van der Waals superlattices, Int. J. Heat Mass Transfer 184, 122390 (2022).
- [34] Z. Fan, H. Dong, A. Harju, and T. Ala-Nissila, Homogeneous nonequilibrium molecular dynamics method for heat transport and spectral decomposition with many-body potentials, Phys. Rev. B **99**, 064308 (2019).
- [35] Z. Chen, M. L. Berrens, K.-T. Chan, Z. Fan, and D. Donadio, Thermodynamics of water and ice from a fast and scalable firstprinciples neuroevolution potential, J. Chem. Eng. Data 69, 128 (2024).
- [36] Two-dimensional ferroelectric crystal with temperatureinvariant ultralow thermal conductivity, https://www.bohrium. com/notebooks/34717712597.
- [37] J. Wu, L. Bai, J. Huang, L. Ma, J. Liu, and S. Liu, Accurate force field of two-dimensional ferroelectrics from deep learning, Phys. Rev. B **104**, 174107 (2021).
- [38] T. Nian, Z. Wang, and B. Dong, Thermoelectric properties of α -In₂Se₃ monolayer, Appl. Phys. Lett. **118**, 033103 (2021).
- [39] G. Han, Z.-G. Chen, J. Drennan, and J. Zou, Indium selenides: Structural characteristics, synthesis and their thermoelectric performances, Small 10, 2747 (2014).

- [40] N. T. Hung, A. R. T. Nugraha, and R. Saito, Two-dimensional InSe as a potential thermoelectric material, Appl. Phys. Lett. 111, 092107 (2017).
- [41] H. Qi, C. Wu, P. Lu, and C. Liu, Phonon thermal transport in ferroelectric α -In₂Se₃ via first-principles calculations, Nanotechnology **35**, 085701 (2024).
- [42] G. Barbalinardo, Z. Chen, N. W. Lundgren, and D. Donadio, Efficient anharmonic lattice dynamics calculations of thermal transport in crystalline and disordered solids, J. Appl. Phys. 128, 135104 (2020).
- [43] X. Tao and Y. Gu, Crystalline-crystalline phase transformation in two-dimensional In₂Se₃ thin layers, Nano Lett. 13, 3501 (2013).
- [44] F. Yang, Q. Zeng, B. Chen, D. Kang, S. Zhang, J. Wu, X. Yu, and J. Dai, Lattice thermal conductivity of MgSiO₃ perovskite and post-perovskite under lower mantle conditions calculated by deep potential molecular dynamics, Chin. Phys. Lett. **39**, 116301 (2022).
- [45] N. Ouyang, Z. Zeng, C. Wang, Q. Wang, and Y. Chen, Role of high-order lattice anharmonicity in the phonon thermal transport of silver halide AgX (X = Cl, Br, I), Phys. Rev. B **108**, 174302 (2023).
- [46] V. D. Camiola, V. Romano, and G. Vitanza, Wigner equations for phonons transport and quantum heat flux, J. Nonlinear Sci. 34, 10 (2024).
- [47] A. Das and P. Banerji, Antibonding or nonbonding interactiondriven phonon modes softening and wave-like interband thermal conduction in layered In₄Te₃ under the framework of Wigner transport formalism, ACS Appl. Energy Mater. **6**, 11521 (2023).
- [48] E. Di Lucente, M. Simoncelli, and N. Marzari, Crossover from Boltzmann to Wigner thermal transport in thermoelectric skutterudites, Phys. Rev. Res. **5**, 033125 (2023).
- [49] A. Pazhedath, L. Bastonero, N. Marzari, and M. Simoncelli, First-principles characterization of thermal conductivity in LaPO₄-based alloys, Phys. Rev. Appl. 22, 024064 (2024).
- [50] J. Liu and S. T. Pantelides, Pyroelectric response and temperature-induced α - β phase transitions in α -In₂Se₃ and other α -III₂VI₃ (III= Al, Ga, In; VI= S, Se) monolayers, 2D Mater. **6**, 025001 (2019).
- [51] C. Xu, Y. Chen, X. Cai, A. Meingast, X. Guo, F. Wang, Z. Lin, T. W. Lo, C. Maunders, S. Lazar, N. Wang, D. Lei, Y. Chai, T. Zhai, X. Luo, and Y. Zhu, Two-dimensional antiferroelectricity in nanostripe-ordered In₂Se₃, Phys. Rev. Lett. 125, 047601 (2020).
- [52] P. S. Thorup, R. B. Stubkjær, K.-K. Huynh, P. Ventrapati, E. S. Vosegaard, A. B. Borup, and B. B. Iversen, Structural origins of ultralow glass-like thermal conductivity in AgGaGe₃Se₈, Sci. Adv. 11, eadv5865 (2025).
- [53] Y. Chen, M. Zhang, D. Li, Y. Tang, H. Ren, J. Li, K. Liang, Y. Wang, L. Wen, W. Li, W. Kong, S. Liu, H. Wang, D. Wang, and B. Zhu, Bidirectional synaptic phototransistor based on two-dimensional ferroelectric semiconductor for mixed color pattern recognition, ACS Nano 17, 12499 (2023).
- [54] P. Umari and A. Pasquarello, *Ab initio* molecular dynamics in a finite homogeneous electric field, Phys. Rev. Lett. **89**, 157602 (2002).

- [55] S. Liu, I. Grinberg, and A. M. Rappe, Intrinsic ferroelectric switching from first principles, Nature (London) 534, 360 (2016).
- [56] T. Swoboda, K. Klinar, A. S. Yalamarthy, A. Kitanovski, and M. M. Rojo, Solid-state thermal control devices, Adv. Electron. Mater. 7, 2000625 (2021).
- [57] B. M. Foley, M. Wallace, J. T. Gaskins, E. A. Paisley, R. L. Johnson-Wilke, J. W. Kim, P. J. Ryan, S. Trolier-McKinstry, P. E. Hopkins, and J. F. Ihlefeld, Voltage-controlled bistable
- thermal conductivity in suspended ferroelectric thin-film membranes, ACS Appl. Mater. Interfaces **10**, 25493 (2018).
- [58] J. Cho, M. D. Losego, H. G. Zhang, H. Kim, J. Zuo, I. Petrov, D. G. Cahill, and P. V. Braun, Electrochemically tunable thermal conductivity of lithium cobalt oxide, Nat. Commun. 5, 4035 (2014).
- [59] G. F. Nataf, S. Volz, J. Ordonez-Miranda, J. Íñiguez González, R. Rurali, and B. Dkhil, Using oxides to compute with heat, Nat. Rev. Mater. 9, 530 (2024).